



MedLSAM: Localize and Segment Anything Model for 3D CT Images

Wenhui Lei^{a,b}, Wei Xu^{c,d}, Kang Li^{b,d}, Xiaofan Zhang^{a,b,*}, Shaoting Zhang^{a,b}

^aSchool of Electronic Information and Electrical Engineering, Shanghai Jiao Tong University, Shanghai, China

^bShanghai AI Lab, Shanghai, China

^cSchool of Biomedical Engineering, Division of Life Sciences and Medicine, University of Science and Technology of China, Hefei, China

^dWest China Biomedical Big Data Center, West China Hospital, Sichuan University, Chengdu, China

ARTICLE INFO

Article history:

Keywords: SAM, Medical Image Segmentation, Contrastive Learning

ABSTRACT

The Segment Anything Model (SAM) has recently emerged as a groundbreaking model in the field of image segmentation. Nevertheless, both the original SAM and its medical adaptations necessitate slice-by-slice annotations, which directly increase the annotation workload with the size of the dataset. We propose MedLSAM to address this issue, ensuring a constant annotation workload irrespective of dataset size and thereby simplifying the annotation process. Our model introduces a 3D localization foundation model capable of localizing any target anatomical part within the body. To achieve this, we develop a Localize Anything Model for 3D Medical Images (MedLAM), utilizing two self-supervision tasks: unified anatomical mapping (UAM) and multi-scale similarity (MSS) across a comprehensive dataset of 14,012 CT scans. We then establish a methodology for accurate segmentation by integrating MedLAM with SAM. By annotating several extreme points across three directions on a few templates, our model can autonomously identify the target anatomical region on all data scheduled for annotation. This allows our framework to generate a 2D bbox for every slice of the image, which is then leveraged by SAM to carry out segmentation. We carried out comprehensive experiments on two 3D datasets encompassing 38 distinct organs. Our findings are twofold: 1) MedLAM is capable of directly localizing any anatomical structure using just a few template scans, yet its performance surpasses that of fully supervised models; 2) MedLSAM not only aligns closely with the performance of SAM and its specialized medical adaptations with manual prompts but achieves this with minimal reliance on extreme point annotations across the entire dataset. Furthermore, MedLAM has the potential to be seamlessly integrated with future 3D SAM models, paving the way for enhanced performance. Our code is public at <https://github.com/openmedlab/MedLSAM>.

© 2023 Elsevier B. V. All rights reserved.

1. Introduction

Recently, there has been an increasing interest in the field of computer vision to develop large-scale *foundational models* that can concurrently address multiple visual tasks, such as image classification, object detection, and image segmenta-

tion. For instance, CLIP (Radford et al., 2021), aligning a vast number of images and text pairs collected from the web, could recognize new visual categories using text *prompts*. Similarly, GLIP (Li et al., 2022; Zhang et al., 2022), which integrates object detection with phrase grounding in pre-training using web-sourced image-text pairs, boasts strong zero-shot and few-shot transferability in object-level detection tasks. On the segmentation front, the *Segment Anything Model (SAM)* (Kirillov et al.,

*Corresponding author: xiaofan.zhang@sjtu.edu.cn

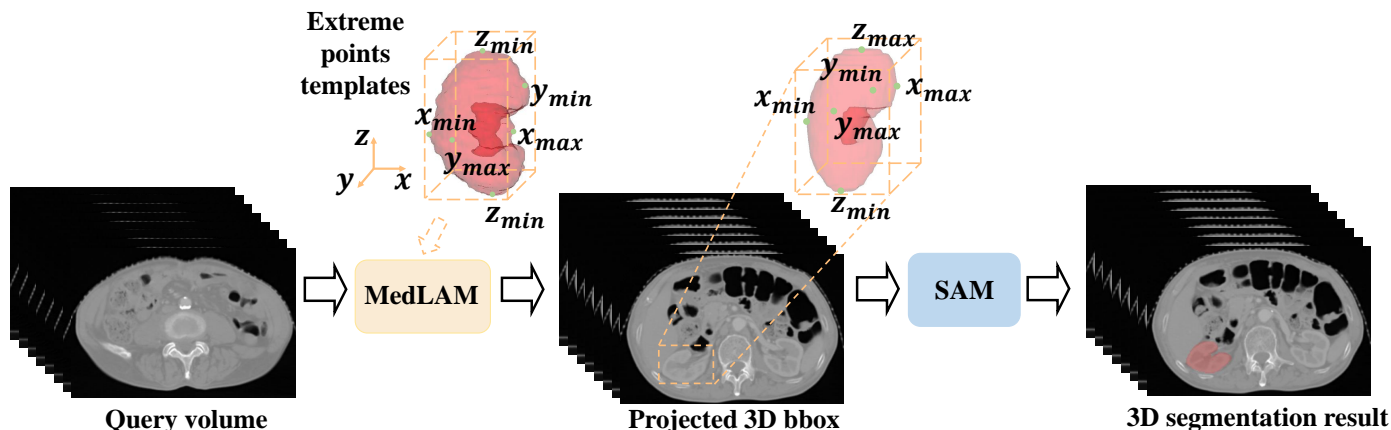


Fig. 1: The overall segmentation pipeline of MedLSAM operates as follows. Given a dataset of any size, MedLSAM first applies a localization process (MedLAM) to identify the six extreme points (in the z , x , and y directions) of any anatomical structure of interest. This process results in the generation of a 3D bbox encompassing the targeted organ or structure. Subsequently, for each slice within this 3D bbox, a 2D bbox is derived, representing the projection of the 3D bbox onto that specific slice. These 2D bboxes are then utilized by the Segment Anything Model (SAM) to carry out precise segmentation of the target anatomy, thereby automating the entire segmentation process.

2023) has recently demonstrated remarkable capabilities in a broad range of segmentation tasks with appropriate prompts, e.g. points, bounding box (bbox) and text.

As foundational models increasingly demonstrate their prowess in general computer vision tasks, the medical imaging domain, characterized by limited image availability and high annotation costs, is taking keen notice of their potential. Such challenges in medical imaging underscore the pressing need for foundational models, drawing greater attention from researchers (Zhang and Metaxas, 2023). Some studies have endeavored to design self-supervised learning tasks tailored to dataset characteristics, pre-training on a vast amount of unlabeled data, and then fine-tuning on specific downstream tasks to achieve commendable results (Wang et al., 2023; Zhou et al., 2023; Vorontsov et al., 2023). In contrast, other works have focused on pre-training with large annotated datasets, either to fine-tune on new tasks (Huang et al., 2023b) or to enable direct segmentation without the necessity of further training or fine-tuning (Butoi et al., 2023). Overall, these models offer myriad advantages: they simplify the development process, reduce dependence on voluminously labeled datasets, and bolster patient data privacy.

In the field of segmentation, models such as SAM and its medical adaptations (Wu et al., 2023; Ma and Wang, 2023; Cheng et al., 2023; He et al., 2023b; Huang et al., 2023a; He et al., 2023a; Zhang and Liu, 2023; Mazurowski et al., 2023; Zhang and Jiao, 2023) have demonstrated significant potential. Both Huang et al. (2023a) and Cheng et al. (2023) have collected extensive medical image datasets and conducted comprehensive testing on SAM. They discovered that, while SAM exhibits remarkable performance on certain objects and modalities, it is less effective or even fails in other scenarios. This inconsistency arises from SAM’s primary training on natural images. To enhance SAM’s generalization in medical imaging, studies like Wu et al. (2023); Ma and Wang (2023) have fine-tuned the original SAM using a large annotated medical image dataset, thereby validating its improved performance over the

base SAM model in test datasets. Despite these advancements, the models still require manual prompts, such as labeled points or bounding boxes, which remains a substantial limitation due to the associated time and financial implications.

In scenarios requiring manual annotation prompts, annotating 3D images proves especially time-consuming and labor-intensive. A single 3D scan often contains dozens or even hundreds of slices. When each slice comprises multiple target structures, the annotation requirements for the entire 3D scan grow exponentially (Wang et al., 2018; Lei et al., 2019). To eliminate this vast annotation demand and facilitate the use of SAM and its medical variants on 3D data, an effective approach would be to automatically generate suitable prompts for the data awaiting annotation. While this could be achieved by training a detector specifically for the categories to be annotated, it introduces the additional burden of annotating data for detector training, and the detectable categories remain fixed (Baumgartner et al., 2021). A more optimal solution would be to develop a universal localization model for 3D medical images. This model would only require users to provide minimal annotations to specify the category of interest, allowing for direct localization of the desired target in any dataset without further training.

However, to the best of our knowledge, foundational models specifically tailored for 3D medical image localization are still limited. In the domain of 2D medical image localization, MIU-VL (Qin et al., 2022) stands out as a pioneering effort. This approach ingeniously marries pre-trained vision-language models with medical text prompts to facilitate object detection in medical imaging. However, the application of these pre-trained models to specialized medical imaging domains, particularly 3D modalities like CT scans, remains challenging. This limitation is attributable to a significant domain gap, as these models were originally trained on 2D natural images.

In response to the lack of localization foundation models for 3D medical images and the persistent need for extensive interaction in SAM, we introduce MedLSAM in this paper.

MedLSAM is an automated medical image segmentation solution that combines the Localize Anything Model for 3D Medical Image (MedLAM), a dedicated 3D localization foundation module designed for localizing any anatomical structure using a few prompts, with existing segmentation foundation models. As illustrated in Fig. 1, MedLSAM employs a two-stage methodology. The first stage involves MedLAM to automatically identify the positions of target structures within volumetric medical images. In the subsequent stage, the SAM model uses the bboxes from the first stage to achieve precise image segmentation. The result is a fully autonomous pipeline that eliminates the need for manual intervention.

The localization foundation model, MedLAM, is an extension of our conference version (Lei *et al.*, 2021) and is premised on the observation that the spatial distribution of organs maintains strong similarities across different individuals. And we assume that there exists a standard anatomical coordinate system, in which the same anatomy part in different people shares similar coordinates. Therefore, we can localize the targeted anatomy structure with a similar coordinate in the unannotated scan. In our previous version, the model was trained separately for different anatomical structures, each using only a few dozen scan images. In contrast, this current study significantly expands the dataset to include 14,012 CT scans from 16 different datasets. This allows us to train a unified, comprehensive model capable of localizing any structure across the entire body. The training process involves a projection network that predicts the 3D physical offsets between any two patches within the same image, thereby mapping every part of the scans onto a shared 3D latent coordinate system.

For the segmentation stage, we employ the original SAM and the well-established MedSAM (Ma and Wang, 2023) as the foundation for our segmentation process. MedSAM, previously fine-tuned on a comprehensive collection of medical image datasets, has exhibited considerable performance in 2D and 3D medical image segmentation tasks. The use of such a robust model bolsters the reliability and effectiveness of our proposed pipeline.

Our contributions can be summarized as follows:

- We introduce MedLSAM, the first completely automated medical adaptation of the SAM model. It not only eliminates the need for manual intervention but also propels the development of fully automated foundational segmentation models in medical image analysis. To the best of our knowledge, this is the first work to achieve complete automation in medical image segmentation by integrating the SAM model;

- Addressing the gap in localization foundation models for 3D medical imaging, we present MedLAM. This model, an extension of our prior conference work (Lei *et al.*, 2021), incorporates pixel-level self-supervised tasks and is trained on a comprehensive dataset of 14,012 CT scans covering the entire body. As a result, it's capable of directly localizing any anatomical structure within the human body and surpassing the fully-supervised model by a significant margin;

- We validate the effectiveness of MedLSAM on two 3D datasets that span 38 organs. As showcased in Table 2, our localization foundation model, MedLAM, exhibits localization

accuracy that not only significantly outperforms existing medical localization foundational models but also rivals the performance of fully-supervised models. Concurrently, as demonstrated in Table 4, MedLSAM aligns with the performance of SAM and its medical adaptations, substantially reducing the reliance on manual annotations. To further the research in foundational models for medical imaging, we have made all our models and codes publicly available.

2. Related Work

2.1. Medical Visual Foundation Models

Over recent years, large-scale pre-trained deep learning vision models have marked remarkable milestones with models like ResNet(He *et al.*, 2016), ConvNeXt(Liu *et al.*, 2022), Vision Transformers (ViT)(Dosovitskiy *et al.*, 2020), and DINO(Caron *et al.*, 2021). Owing to their profound representational power and exceptional generalization capabilities, these models have consistently excelled in various downstream applications.

In the realm of medical image analysis, the challenges are compounded by concerns of data privacy and the often tedious nature of annotation tasks, making the procurement of large-scale annotated data both challenging and costly. This elevates the significance of visual foundational models in the field. For instance, REMEDIS(Azizi *et al.*, 2022) harnesses the potential of self-supervised learning on a diverse set of medical images spanning multiple modalities. Impressively, it rivals the performance of heavily supervised baselines in downstream disease classification tasks, requiring only between 1% to 33% of the typical retraining data. Meanwhile, SAIS(Azizi *et al.*, 2022), capitalizing on the foundational model DINO(Caron *et al.*, 2021) pre-trained on standard images, showcases impressive generalization and prowess in specialized tasks, such as surgical gesture recognition and skill evaluation.

Turning the attention to segmentation, a key aspect within medical imaging, there has been a surge of interest in the application of SAM for medical image segmentation (Cheng *et al.*, 2023; He *et al.*, 2023b; Wu *et al.*, 2023; Ma and Wang, 2023; Huang *et al.*, 2023a; He *et al.*, 2023a; Zhang and Liu, 2023; Mazurowski *et al.*, 2023; Zhang and Jiao, 2023). Notably, with additional medical data collected for fine-tuning, the medical adaptations tailored for SAM, specifically Wu *et al.* (2023); Ma and Wang (2023), have exhibited commendable results in this domain.

However, a significant hurdle for SAM's utility in medical image segmentation is the necessity for manual annotations. This involves annotating specific points or bboxes that demarcate the segmentation region, a process that is both time-consuming and expensive. Intriguingly, comprehensive studies by Huang *et al.* (2023a) and Cheng *et al.* (2023) have delved into the optimal prompts for SAM's application in medical imaging. They primarily investigated prompt types including bboxes, a combination of bboxes with foreground and background points, and the exclusive use of foreground and background points. Notably, in the majority of tasks, bboxes alone showcased superior performance.

In light of these findings, one of the central focuses of this paper is the automation of generating bbox prompts for SAM. Furthermore, we aim to advance the full automation of SAM’s application in the medical domain, reducing the reliance on manual annotations and propelling its utility.

2.2. Medical Localization Models

Traditionally, localization tasks, such as object detection, have relied on extensive annotations for a limited set of categories to enable models to produce corresponding bboxes (Redmon et al., 2016; He et al., 2017; Dai et al., 2016; Ren et al., 2015). This challenge has also been extensively addressed in the realm of medical imaging, with a focus on areas such as organ localization (Xu et al., 2019; Navarro et al., 2020; Hussain et al., 2021; Navarro et al., 2022), keypoint detection (Chen et al., 2021; Wan et al., 2023), and lesion detection (Yan et al., 2018; Zhang et al., 2018). Both organ localization and keypoint detection often serve as preliminary steps for many medical image analysis tasks, including image registration (Sun et al., 2013), organ segmentation (Liu et al., 2023), and disease diagnosis (Bilic et al., 2023). While previous fully-supervised models have achieved commendable results in predefined tasks, their primary limitation is their difficulty in generalizing to new categories. The high cost and challenges associated with data collection and annotation further exacerbate this issue, especially pronounced in the field of medical imaging.

To reduce annotation costs, our previous work, the Relative Position Regression-Net (RPR-Net) (Lei et al., 2021), along with another study, Cascade Comparing to Detect (CC2D) (Yao et al., 2021), pioneered the localization of regions of interest or landmarks using annotations from just a single instance. Specifically, CC2D learns to project pixels associated with the same anatomical structures into embeddings with high cosine similarities by addressing a self-supervised “patch matching” proxy task in a coarse-to-fine manner. However, both RPR-Net and CC2D were trained on limited datasets as independent models, without evolving into foundational models for localization.

3. Method

As illustrated in Fig. 1, MedLSAM comprises two core components: the automated localization algorithm MedLAM and the automated segmentation algorithm SAM. In the subsequent sections, we first delve into the architecture and training of MedLAM. Following that, we detail how MedLAM synergizes with SAM to realize the complete autonomous segmentation framework.

3.1. Training of MedLAM

Our MedLAM model, depicted in Fig. 2, consists of three primary modules: a feature encoder, a multilayer perceptron (MLP), and a feature decoder. Both the feature encoder and decoder are composed of four convolutional blocks. The encoder blocks each have two convolutional layers followed by a downsampling layer, while the decoder blocks contain two convolutional layers succeeded by an upsampling layer. The MLP is structured with three fully connected layers.

We start by selecting a volumetric image \mathbf{v} from the unannotated training set. We then extract two large image patches from \mathbf{v} , which serve as the source for further extractions. These large patches undergo a variety of transformations to produce two pairs of patches, namely, the original patch pair $\mathbf{x}_q, \mathbf{x}_s \in R^{D \times W \times H}$ and the augmented patch pair $\mathbf{x}'_q, \mathbf{x}'_s \in R^{D \times W \times H}$. The augmentation techniques employed include rotation, elastic transformations, and the addition of random noise. Our training objectives are twofold: 1) **Unified Anatomical Mapping (UAM)**: To project scan images from different individuals onto a shared anatomical coordinate space by predicting the relative distance between the original image patches \mathbf{x}_q and \mathbf{x}_s . 2) **Multi-Scale Similarity (MSS)**: Ensure that the similarity between features corresponding to the same region is maximized in both the original image patches $\mathbf{x}_q, \mathbf{x}_s$ and their augmented counterparts $\mathbf{x}'_q, \mathbf{x}'_s$.

3.1.1. Unified Anatomical Mapping (UAM)

In this step, we introduce the Unified Anatomical Mapping (UAM) framework, building upon the foundation of our earlier methodology (Lei et al., 2021). The central principle remains consistent: mapping 3D scan images from diverse individuals onto a unified implicit 3D anatomical coordinate system. By doing so, identical anatomical structures from various individuals can be associated with the same coordinate, facilitating an initial, coarse localization of the point within the unannotated scan corresponding to our point of interest.

In contrast to our prior endeavors, UAM embodies a broader vision of creating a model that captures the underlying anatomical structures across a wide range of human body scans. While our previous methods primarily focused on training specialized models for individual localized scan datasets, the UAM framework takes advantage of an extensive collection of CT scans, covering the entire human spectrum. This approach aims to provide a more holistic model capable of operating seamlessly across different organs and body regions, increasing the versatility and applicability of our method but also ensuring higher accuracy and reliability in diverse medical contexts.

The RDR model aims to predict the 3D offset between the query patch \mathbf{x}_q and the support patch \mathbf{x}_s . Considering $\mathbf{e} \in R^3$ as the pixel spacing of \mathbf{v} , and $\mathbf{c}_q, \mathbf{c}_s \in R^3$ as the centroid coordinates of \mathbf{x}_q and \mathbf{x}_s in \mathbf{v} respectively, the ground truth offset \mathbf{d}'_{qs} from \mathbf{x}_q to \mathbf{x}_s in the physical space can be calculated as:

$$\mathbf{d}'_{qs} = (\mathbf{c}_s - \mathbf{c}_q) \cdot \mathbf{e}. \quad (1)$$

Both \mathbf{x}_s and \mathbf{x}_q undergo processing via the feature encoder to distill high-level features. Subsequently, MLP maps these features to their corresponding 3D latent vectors, \mathbf{p}_s and $\mathbf{p}_q \in R^3$. This process leads to the predicted offset $\mathbf{d}_{qs} \in R^3$ from the query patch \mathbf{x}_q to the support patch \mathbf{x}_s being computed as:

$$\mathbf{d}_{qs} = r \cdot \tanh(\mathbf{p}_s - \mathbf{p}_q). \quad (2)$$

The utilization of the hyperbolic tangent function \tanh in conjunction with the hyper-parameter r is intended to dictate the upper and lower bound of \mathbf{d}_{qs} , thereby covering the largest feasible offset. Lastly, to measure the difference between \mathbf{d}_{qs}

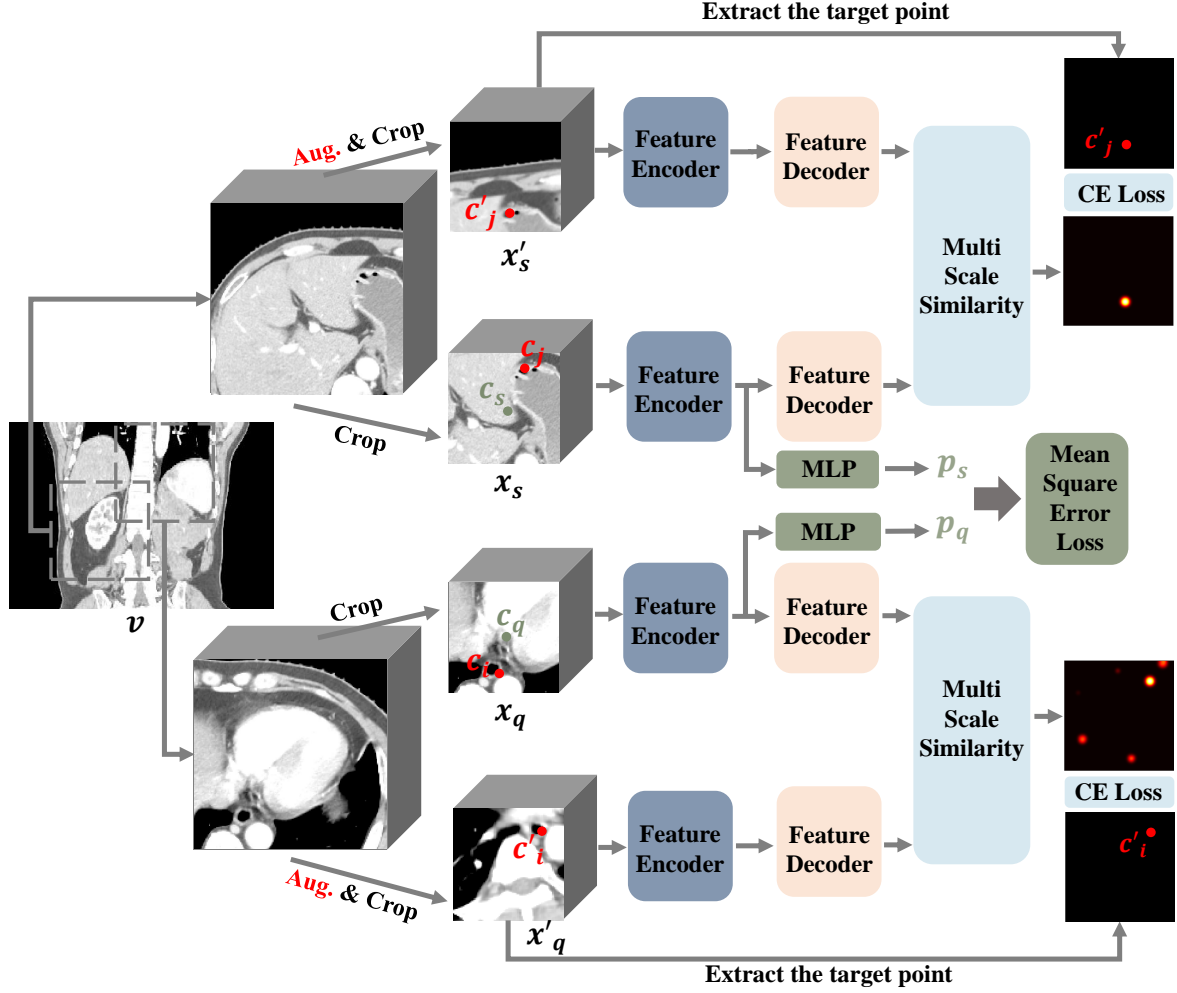


Fig. 2: The learning process of MedLAM.

and d'_{qs} , we employ the Mean Square Error (MSE) loss function:

$$L_{MSE} = \|d_{qs} - d'_{qs}\|^2. \quad (3)$$

Owing to the constraints set by the hyper-parameter r and the inherent anatomical similarities across different individuals, the model effectively projects the same anatomical regions from various individuals onto similar implicit coordinates after training. This projection mechanism aids in achieving a consistent and unified representation across diverse datasets, thereby enhancing the adaptability and precision of our MedLAM model.

3.1.2. Multi Scale Similarity (MSS)

However, given the inherent variations in anatomical positioning across different individuals, regions sharing the same latent coordinates in various images may still correspond to different anatomical structures. Therefore, we need to further refine the precision of our localization by extracting local pixel-level features from our points of interest. This allows us to pinpoint the most similar feature within the vicinity of the initially localized point, thereby enhancing the overall localization accuracy. This is inspired by the work in Cascade Comparing to Detect (CC2D) (Yao et al., 2021), which ensures that augmented

instances of the same image yield highly similar features for the same point, while different points exhibit substantially divergent features.

More specifically, as illustrated in Fig. 3, the inputs to our MSS process encompass normalized multi-scale feature maps, denoted as $F = \{F^i, i = 0, 1, 2\}$ and $F' = \{F'^i, i = 0, 1, 2\}$, extracted from x and x' , respectively. These multi-scale feature maps consist of three different scales, where the size of each scale is $1/2^i$ times the size of the original image, with the largest scale being the same size as the original image.

Given a chosen point c_j from x , which has a corresponding point in x' is denoted as c'_j . For every scale i of the multi-scale feature maps, we extract the feature vectors $f_{c_j}^i$ and $f_{c'_j}^i$ corresponding to points c_j and c'_j respectively. Formally, $f_{c_j}^i = F^i(c_j)$ and $f_{c'_j}^i = F'^i(c'_j)$.

To compute the similarity between these feature vectors and the corresponding scale feature maps in x' , we use the cosine similarity metric. The cosine similarity s between two vectors a and b is given by:

$$s(a, b) = \frac{a \cdot b}{\|a\|_2 \cdot \|b\|_2}. \quad (4)$$

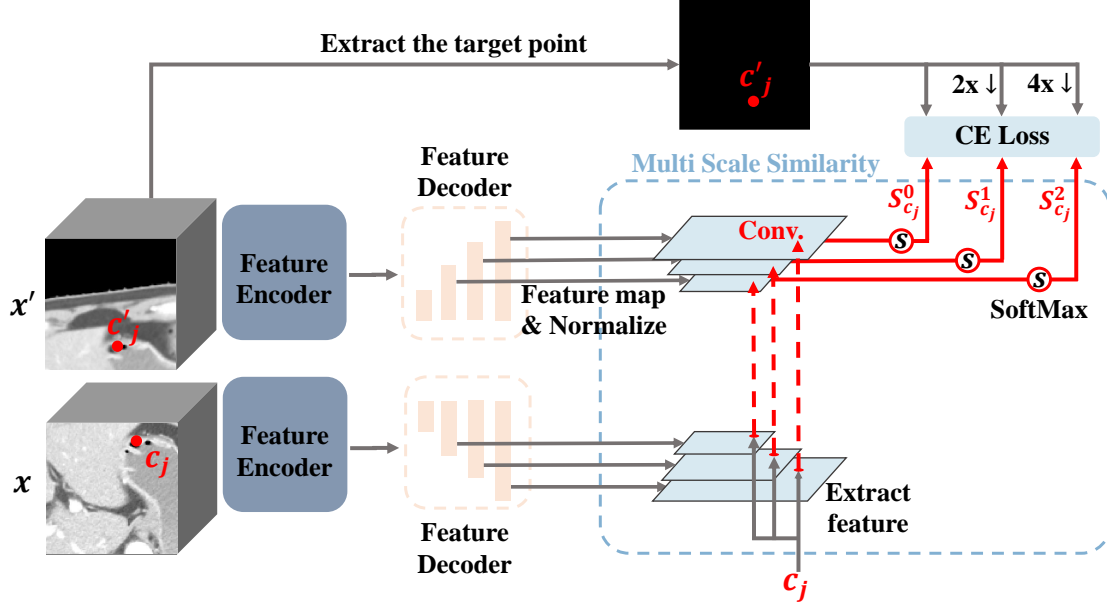


Fig. 3: Details of the Multi Scale Similarity (MSS).

Since the F^i and $F^{i'}$ are both normalized, for each scale i , the cosine similarity map is computed by using the feature vector $f_{c'_j}^i$ as a $1 \times 1 \times 1$ convolutional kernel that operates on the corresponding feature map from the augmented image. Our optimization objective is to increase the similarity between $f_{c'_j}^i$ and $f_{c_j}^i$ relative to other points, effectively enhancing their mutual likeness while diminishing their similarity to the remaining features in the augmented image. To achieve this, we apply the softmax operation across all values in the cosine similarity map, resulting in the final probability map $S_{c_j}^i$. Correspondingly, the ground truth $Y_{c_j}^i$ at scale i , is set as:

$$Y_{c_j}^i(c) = \begin{cases} 1, & \text{if } c = \text{round}(\frac{c'_j}{2^i}) \\ 0, & \text{otherwise} \end{cases} \quad (5)$$

This ensures that all other points are set to 0, while the corresponding position for c'_j at scale i is set to 1. We utilize the Cross Entropy (CE) loss to align each $S_{c_j}^i$ with its corresponding ground truth $Y_{c_j}^i$:

$$L_{CE} = \sum_i -Y_{c_j}^i \cdot \log(S_{c_j}^i) - (1 - Y_{c_j}^i) \cdot \log(1 - S_{c_j}^i). \quad (6)$$

Eventually, we set the final loss function as:

$$L_{SSL} = L_{MSE} + L_{CE}. \quad (7)$$

3.2. Inference of MedLSAM

In this section, we will elaborate on the process of utilizing MedLAM to localize any point of interest within scans. Additionally, we further elucidate the mechanism through which MedLAM crafts 3D bbox prompts for the anatomical structures of interest. These 3D prompts are then sliced into 2D bboxes corresponding to each layer of the structure. Each 2D bbox,

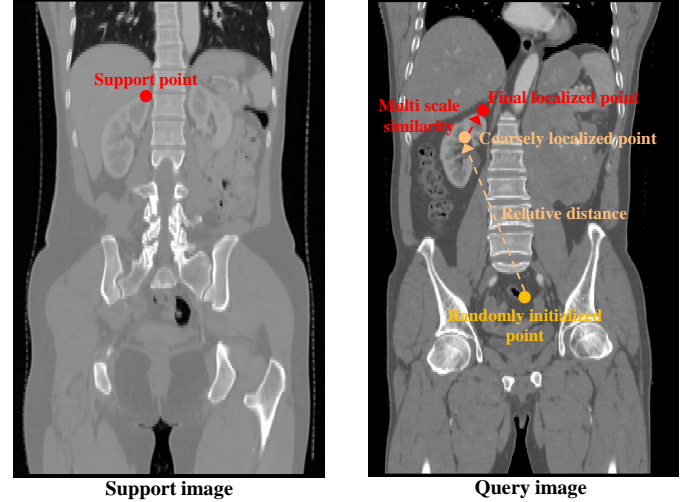


Fig. 4: Structure of the inference stage in the Medical Localization Anything Model (MedLAM). The process involves moving an agent from a randomly initialized position toward the target landmark, guided by 3D relative distance and multi-scale feature vectors.

acting as a prompt for its respective layer, is combined with the corresponding image slice and processed by the SAM model to produce the segmentation results.

3.2.1. Landmark Localization

As posited in Section 3.1.1, we assume that the same anatomical structure in different individuals corresponds to the same latent coordinates. This allows us to calculate the latent coordinates of any point within the query volume and subsequently determine its relative distance to the target landmark by computing the difference in their latent coordinates.

As shown in Fig. 4, we conceptualize the localization task as moving an agent from a randomly initialized position in the

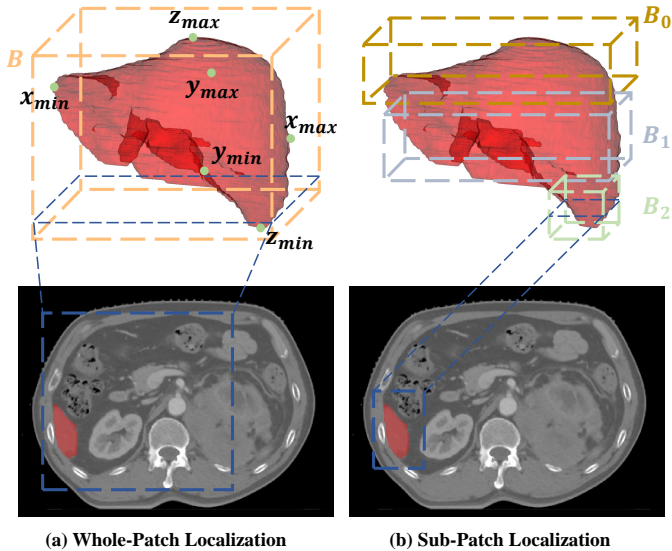


Fig. 5: Comparison between Whole-Patch Localization (WPL) and Sub-Patch Localization (SPL) strategies. (a) WPL generates a single minimal 3D bounding box (B) by identifying the six extreme points of the target anatomical structure. (b) SPL divides the target structure into multiple segments, each with its own localized 3D bounding box (B_i), resulting in a more accurate representation at each slice.

query image toward the target location. A patch is extracted from a random position within the query image, and simultaneously, a support patch is extracted from the support image, centered around the pre-specified landmark. Upon processing these two patches through the MedLAM model, we obtain a 3D offset that represents the estimated relative spatial displacement between the start and target positions and the multi-scale feature vectors of the pre-specified landmark. By updating the agent’s location based on this offset, we achieve a coarse localization of the landmark within the query image.

To further refine the landmark localization, we employ the Multi-Scale Similarity (MSS) component of MedLAM. Specifically, we extract a 3D patch of size $D \times W \times H$ centered around the coarsely localized point in the query image. Within the extracted patch, we compute multi-scale feature maps, perform similarity calculations, and aggregate the resulting similarity maps. This allows us to identify the location within the patch that exhibits the highest feature similarity, thereby significantly enhancing the precision of our landmark localization.

3.2.2. Sub-Patch Localization (SPL)

As shown in Fig. 5(a), for a target anatomical structure, we can generate a single minimal 3D bounding box (bbox) B that completely encompasses the organ by locating its six extreme points in three dimensions: $[z_{min}, z_{max}, x_{min}, x_{max}, y_{min}, y_{max}]$. We call this localization approach as **Whole-Patch Localization (WPL)**. However, the cross-sectional area of this 3D bbox on each layer may significantly exceed the actual cross-sectional area of the organ at that layer, resulting in highly inaccurate bbox prompts.

In response, we introduce the **Sub-Patch Localization (SPL)** strategy. Rather than using a single bounding box, SPL divides the target structure into multiple segments, each seg-

ment having its own dedicated 3D bbox, denoted as B_i . This segmented approach, as visualized in Fig. 5(b), ensures that each bbox is tailored to more accurately represent the organ’s actual cross-sectional area at every layer.

Delving into the specifics, for any given target organ, SPL slices the organ into segments at intervals of n mm, resulting in m distinct segments for the organ. Consequently, MedLAM is then tasked with localizing these m segments in the query volume, producing m individual bounding boxes: $[z_{min}^i, z_{max}^i, x_{min}^i, x_{max}^i, y_{min}^i, y_{max}^i]$ for each segment i . This refined approach provides a much more accurate spatial representation of the anatomical structure across its entirety.

3.2.3. SAM Segmentation

After generating the bbox prompts for each slice, we transition to the segmentation stage. For this, we utilize both SAM and MedSAM, a specialized variant of SAM that has been fine-tuned for medical image datasets. Both models serve as the foundation for our segmentation tasks. The versatility of SAM and the domain-specific adaptations of MedSAM help us provide robust segmentation results, thereby adding to the overall efficacy of the MedSLAM system.

4. Experiments

4.1. Dataset

Our MedLAM model is trained on an extensive set of 16 datasets, which collectively comprise a total of 14,012 CT scans. These scans encompass various regions of the human body, providing comprehensive anatomical coverage. An overview of the training datasets is provided in Table 1. The diverse and abundant training data ensures the robustness and generalizability of our model across different medical imaging contexts.

To validate the effectiveness of our approach, we integrate MedLAM with two segmentation backbones: SAMKirillov et al. (2023) and MedSAMMA and Wang (2023). We test these combined models on two CT segmentation datasets: 1) StructSeg19 Task1 dataset¹ for the 22 Head-and-Neck (HaN) organs with 50 scans; 2) the WORD dataset Luo et al. (2022) for the 16 abdomen organs with 120 scans.

4.2. Implementation Details

Our model was trained using four NVIDIA GTX 3090 Ti GPUs. We utilized the Adam optimizer Kingma and Ba (2014) with a batch size of 8, an initial learning rate of 10^{-3} , and a training duration of 250 epochs.

In terms of pre-processing for MedLAM’s training and inference, we rescaled the voxel spacing to $[3,3,3]$ mm and standardized the cropping patch sizes to $64 \times 64 \times 64$ pixels. To ensure that the scanning range was fully covered, we set the parameter r as $[1500, 600, 600]$.

¹<https://structseg2019.grand-challenge.org/Home/>

Table 1: Detailed information of the 16 CT datasets for MedLAM training.

Dataset	Number	Anatomical Region
GLIA Bo et al. (2021)	1338	HaN
ACRIN 6685Lowe et al. (2019)	260	HaN
OPC-RadiomicsKwan et al. (2018)	606	HaN
Head-Neck-PET-CTVallieres et al. (2017)	298	HaN
HNSCC Grossberg et al. (2018)	591	HaN/Thorax/Abdomen
autoPET Gatidis et al. (2022)	1014	Whole
MELA Chen (2022)	770	Thorax
LIDC-IDRIArmato III et al. (2011)	1308	Thorax
STOIC2021Revel et al. (2021)	2000	Thorax
MSD-LungAntonelli et al. (2022)	95	Thorax
CBIS-DDSMLee et al. (2017)	2620	Thorax
AMOS 2022Ji et al. (2022)	500	Thorax/Abdomen
Kits19Heller et al. (2020)	141	Abdomen
MSD-ColonAntonelli et al. (2022)	190	Abdomen
MSD-PancreasAntonelli et al. (2022)	281	Abdomen
FLARE2022Ma et al. (2022)	2000	Abdomen
Total	14,012	Whole

In both the StructSeg HaN and WORD datasets, we start by randomly selecting 5 scans as support volumes. In the Whole-Patch Localization (WPL) approach, for each organ in these scans, we compute the six extreme coordinates and then average these coordinates and features across the 5 selected images. This creates an average representation of latent coordinates and features for each of the organ’s extreme points.

When employing Sub-Patch Localization (SPL), we deviate from this process. Instead of focusing on the extreme coordinates of the organ, we divide each target organ into a number of sub-patches, denoted as i . The value of i is determined by taking the minimum span of the target organ across all support volumes and dividing it by the predefined patch distance n mm. This ensures that we have a consistent number of sub-patches for each target organ across all support volumes. For each of these i sub-patches, we crop, compute, and integrate the latent coordinates and features across the 5 support volumes, offering a more granular representation. As a result, we obtain the latent coordinates and features for $6i$ points.

Upon obtaining the latent coordinates and features for each target point, we proceed to locate the corresponding 3D bounding boxes (bbox) in the query volume, yielding a bbox for each slice, as elaborated in Sec. 3.2. To accommodate for potential variations in organ size and shape, we extend each slice’s bbox prompt by $[10, 10]$ pixels in the x and y directions, respectively. This allows us to ensure that the entire target structure is adequately captured for subsequent processing.

Upon utilizing SAM and MedSAM, the original images are subjected to a separate preprocessing routine in line with the standard procedures described in the original MedSAM methodology. This includes adjusting the slice resolution to $3 \times 1024 \times 1024$, normalizing the intensity.

To guarantee the robustness of our experimental results, we repeat this random selection and averaging process five times. The final performance metrics are obtained by averaging the outcomes of these iterations.

4.3. Evaluation Metrics

To evaluate the localization accuracy of MedLAM, we apply two widely utilized metrics (Humpire-Mamani et al., 2018; Xu

et al., 2019; Lei et al., 2021): the Intersection over Union (IoU) and Wall Distance (WD). The IoU overlap ratio is defined as:

$$IoU = \frac{V_p \cap V_{gt}}{V_p \cup V_{gt}}, \quad (8)$$

where V_p and V_{gt} denote the volume of the predicted bbox and the ground-truth bbox, respectively. The IoU metric (0-1, 0: mismatch; 1: perfectly match) is employed to assess the relative accuracy of the predicted bounding box with respect to the ground truth.

For Wall Distance (WD), it quantifies the average absolute distance difference between the boundaries of the predicted bbox and the ground-truth bbox. Specifically, it is defined as:

$$WD = \frac{1}{6} \sum |d_{p,i} - d_{gt,i}|, \quad (9)$$

where $d_{p,i}$ and $d_{gt,i}$ are the distances of the six boundaries (top, bottom, left, right, front, back) of the predicted and ground-truth bbox, respectively. The pixel spacing is implicitly taken into account in the distance measurement.

As for the segmentation metrics, we use Dice Similarity Coefficient (DSC) score and 95% Hausdorff Distance (HD₉₅) as evaluation metrics to quantitatively evaluate our method. Dice score (0-1, 0: mismatch; 1: perfectly match) measures the overlap of the prediction \mathbf{A} and ground truth \mathbf{B} , and is defined as:

$$DSC(\mathbf{A}, \mathbf{B}) = \frac{2|\mathbf{A} \cap \mathbf{B}|}{|\mathbf{A}| + |\mathbf{B}|} \cdot 100\% \quad (10)$$

The maximum Hausdorff Distance is the maximum distance of a set \mathbf{A} to the nearest point in the other set \mathbf{B} , defined as:

$$d_H(\mathbf{A}, \mathbf{B}) = \max\{\max_{a \in \mathbf{A}} \min_{b \in \mathbf{B}} d(a, b), \max_{b \in \mathbf{B}} \min_{a \in \mathbf{A}} d(a, b)\} \quad (11)$$

HD₉₅ is similar to maximum HD, and it is based on the calculation of the 95th percentile of the distances between boundary points in \mathbf{A} and \mathbf{B} .

4.4. Evaluation of MedLAM

4.4.1. Comparison with Other Methods

In this section, with the purpose of validating the performance of our universal localization model MedLAM. We have conducted a comparative analysis between MedLAM and two well-established methodologies in the medical image detection field: 1) nnDetection Baumgartner et al. (2021), which serves as a highly robust fully-supervised medical image detection baseline; 2) MIU-VL Qin et al. (2023), a pioneer work utilizing visual-language foundation model for zero-shot medical image localization.

For nnDetection, we followed the automated data processing strategy and performed five-fold cross-training approach to identify the optimal network hyperparameters. Regarding MIU-VL, we follow the procedures outlined in the original paper, using GLIP (Li et al., 2022) as the foundation model for zero-shot detection. In order to generate the required text prompts for MIU-VL, we utilized ChatGPT (Ouyang et al., 2022) to generate prompts containing descriptions of

Table 2: MedLAM v.s. fully-supervised & zero-shot localization models on StructSeg Head-and-Neck and WORD datasets.

(a) StructSeg Head-and-Neck						
Organs	IoU \uparrow (mean \pm std %)			WD \downarrow (mean \pm std mm)		
	MedLAM (5-shot)	nnDetection (fully-supervised)	MIU-VL (zero-shot)	MedLAM (5-shot)	nnDetection (fully-supervised)	MIU-VL (zero-shot)
Brain Stem	70.3 \pm 8.0	75.7 \pm 6.4	0.1 \pm 0.0	2.4 \pm 1.4	8.5 \pm 11.9	223.0 \pm 74.3
Eye L	66.2 \pm 11.5	29.0 \pm 35.8	0.0 \pm 0.0	1.7 \pm 1.0	7.2 \pm 13.5	162.8 \pm 73.9
Eye R	63.2 \pm 11.2	42.7 \pm 28.4	0.0 \pm 0.0	1.8 \pm 1.1	8.0 \pm 10.6	163.4 \pm 61.1
Lens L	11.5 \pm 11.0	10.2 \pm 16.0	0.0 \pm 0.0	1.9 \pm 1.1	13.8 \pm 19.5	220.2 \pm 89.7
Lens R	17.9 \pm 14.5	24.3 \pm 22.2	0.0 \pm 0.0	1.8 \pm 1.2	16.8 \pm 19.9	219.1 \pm 75.6
Opt Nerve L	29.7 \pm 27.0	15.4 \pm 15.6	0.0 \pm 0.0	2.0 \pm 1.3	9.5 \pm 14.9	173.0 \pm 56.3
Opt Nerve R	27.6 \pm 25.4	23.6 \pm 17.1	0.0 \pm 0.0	2.1 \pm 1.3	16.2 \pm 18.5	175.7 \pm 47.8
Opt Chiasma	9.7 \pm 19.4	32.4 \pm 9.4	0.5 \pm 0.0	2.8 \pm 1.5	9.0 \pm 13.0	177.0 \pm 25.2
Temporal Lobes L	70.9 \pm 8.7	45.3 \pm 37.1	0.5 \pm 0.1	3.2 \pm 1.8	17.0 \pm 21.0	163.3 \pm 33.9
Temporal Lobes R	72.8 \pm 10.3	26.8 \pm 33.8	0.0 \pm 0.2	3.1 \pm 1.8	9.5 \pm 14.8	189.0 \pm 64.9
Pituitary	8.9 \pm 18.5	25.6 \pm 16.8	0.3 \pm 0.0	2.7 \pm 1.6	24.4 \pm 19.5	229.2 \pm 84.7
Parotid Gland L	63.1 \pm 9.6	31.3 \pm 32.9	0.3 \pm 0.1	3.7 \pm 1.9	11.8 \pm 15.5	162.7 \pm 40.2
Parotid Gland R	62.7 \pm 10.3	38.7 \pm 32.0	0.0 \pm 0.1	4.0 \pm 2.1	13.6 \pm 20.8	170.1 \pm 44.6
Inner Ear L	35.6 \pm 8.2	34.1 \pm 25.2	0.0 \pm 0.0	2.5 \pm 1.0	10.3 \pm 12.2	182.3 \pm 34.8
Inner Ear R	33.7 \pm 9.4	32.1 \pm 27.7	0.1 \pm 0.0	2.7 \pm 1.1	15.3 \pm 16.9	185.4 \pm 28.0
Mid Ear L	56.5 \pm 12.9	31.0 \pm 32.9	0.1 \pm 0.1	3.4 \pm 2.0	14.0 \pm 15.7	193.6 \pm 72.0
Mid Ear R	56.5 \pm 12.8	51.1 \pm 27.5	0.0 \pm 0.1	3.5 \pm 2.1	15.0 \pm 17.1	204.6 \pm 77.5
TM Joint L	40.7 \pm 15.1	26.8 \pm 22.3	0.0 \pm 0.0	2.4 \pm 1.3	11.3 \pm 13.9	188.8 \pm 57.6
TM Joint R	38.7 \pm 15.3	26.0 \pm 18.4	0.5 \pm 0.0	2.3 \pm 1.2	21.4 \pm 21.4	200.2 \pm 64.7
Spinal Cord	57.7 \pm 16.7	10.4 \pm 14.8	0.9 \pm 0.2	2.7 \pm 1.9	11.3 \pm 15.1	224.5 \pm 120.1
Mandible L	80.9 \pm 6.2	36.1 \pm 37.3	1.0 \pm 0.3	2.5 \pm 1.6	13.8 \pm 17.7	164.2 \pm 73.1
Mandible R	80.8 \pm 5.9	34.3 \pm 40.0	1.0 \pm 0.4	2.6 \pm 1.5	21.4 \pm 20.4	155.2 \pm 59.6
Average	48.0 \pm 13.1	31.9 \pm 25.0	0.2 \pm 0.1	2.6 \pm 1.5	13.6 \pm 16.5	187.6 \pm 61.8

(b) WORD						
Organs	IoU \uparrow (mean \pm std %)			WD \downarrow (mean \pm std mm)		
	MedLAM (5-shot)	nnDetection (fully-supervised)	MIU-VL (zero-shot)	MedLAM (5-shot)	nnDetection (fully-supervised)	MIU-VL (zero-shot)
Liver	73.0 \pm 11.6	52.7 \pm 10.2	10.6 \pm 2.1	10.5 \pm 9.1	23.8 \pm 31.5	80.4 \pm 37.2
Spleen	70.9 \pm 13.3	38.2 \pm 17.5	1.7 \pm 1.0	5.7 \pm 5.9	14.6 \pm 21.4	142.5 \pm 49.8
Kidney L	71.0 \pm 15.9	69.6 \pm 27.2	0.9 \pm 0.5	5.0 \pm 8.4	13.9 \pm 22.1	164.3 \pm 69.2
Kidney R	76.0 \pm 13.8	74.2 \pm 11.5	0.8 \pm 0.2	3.6 \pm 4.6	20.8 \pm 28.6	166.1 \pm 81.3
Stomach	49.1 \pm 14.3	36.3 \pm 23.3	4.7 \pm 2.1	17.7 \pm 12.8	17.0 \pm 25.1	102.8 \pm 25.1
Gallbladder	12.0 \pm 11.0	29.3 \pm 18.2	0.2 \pm 0.2	16.9 \pm 10.3	21.2 \pm 29.6	153.2 \pm 38.5
Esophagus	44.2 \pm 17.9	58.5 \pm 13.2	0.3 \pm 0.2	6.8 \pm 6.7	16.8 \pm 18.9	153.8 \pm 22.7
Pancreas	44.1 \pm 17.3	53.4 \pm 17.6	1.6 \pm 0.6	12.2 \pm 8.8	19.1 \pm 28.5	135.2 \pm 33.8
Duodenum	44.5 \pm 17.5	42.0 \pm 16.4	1.2 \pm 0.4	12.7 \pm 9.1	20.5 \pm 26.1	139.8 \pm 31.0
Colon	67.0 \pm 13.0	28.5 \pm 10.9	17.9 \pm 4.4	15.6 \pm 11.8	22.8 \pm 35.8	83.3 \pm 33.6
Intestine	62.6 \pm 11.0	24.6 \pm 10.7	12.2 \pm 4.6	15.4 \pm 9.8	20.5 \pm 29.5	106.0 \pm 53.1
Adrenal	40.4 \pm 17.7	57.3 \pm 12.7	0.4 \pm 0.2	7.6 \pm 5.5	16.1 \pm 26.6	160.2 \pm 58.0
Rectum	49.3 \pm 15.3	62.6 \pm 16.9	0.6 \pm 0.3	8.6 \pm 6.1	17.4 \pm 24.6	203.1 \pm 146.3
Bladder	55.4 \pm 16.9	63.0 \pm 17.0	1.2 \pm 0.7	8.1 \pm 7.6	24.1 \pm 33.2	167.7 \pm 96.9
Head of Femur L	76.7 \pm 16.7	20.0 \pm 26.8	1.6 \pm 2.4	5.3 \pm 16.0	14.5 \pm 23.0	175.1 \pm 127.4
Head of Femur R	69.4 \pm 14.4	47.7 \pm 34.0	1.5 \pm 0.8	5.9 \pm 6.9	23.8 \pm 41.5	163.4 \pm 117.5
Average	56.6 \pm 14.8	47.4 \pm 17.8	3.6 \pm 1.3	9.9 \pm 8.7	19.2 \pm 27.9	143.6 \pm 63.8

[COLOR], [SHAPE], [LOCATION], and [CLASS] for different organs. Since the MIU-VL network is designed to directly handle 2D images, we performed the detection process on 3D

medical images slice by slice. Subsequently, we reconstructed the obtained bounding boxes back into the 3D image space.

The final experimental results are presented in Table 2. Med-

Table 3: Ablation study of Unified Anatomical Mapping (UAM) and Multi Scale Similarity (MSS) in MedLAM: IoU score (mean \pm std%) on the WORD dataset

Organs	UAM	\times	UAM	UAM	UAM	UAM	UAM	UAM	UAM
	+	+	+	+	+	+	+	+	+
	\times	$F^2 + F^1 + F^0$	F^2	F^1	F^0	$F^1 + F^0$	$F^2 + F^0$	$F^2 + F^1$	$F^2 + F^1 + F^0$
Liver	57.1 \pm 10.5	39.7 \pm 27.4	76.0 \pm 8.3	76.7 \pm 7.9	71.5 \pm 10.1	75.0 \pm 09.1	78.5 \pm 7.7	76.6 \pm 7.7	73.0 \pm 11.6
Spleen	40.1 \pm 7.7	49.3 \pm 34.2	63.0 \pm 15.7	72.1 \pm 16.0	69.1 \pm 21.7	74.7 \pm 15.2	74.4 \pm 14.1	72.6 \pm 12.9	70.9 \pm 13.3
Kidney L	45.9 \pm 11.4	39.9 \pm 30.7	60.5 \pm 10.4	58.9 \pm 19.4	52.1 \pm 23.4	54.5 \pm 22.9	64.8 \pm 16.4	63.7 \pm 14.8	71.0 \pm 15.9
Kidney R	40.4 \pm 9.3	40.6 \pm 34.6	62.7 \pm 12.1	68.2 \pm 14.4	54.4 \pm 27.8	73.0 \pm 13.1	76.3 \pm 8.9	70.6 \pm 9.4	76.0 \pm 13.8
Stomach	38.7 \pm 12.2	25.4 \pm 21.9	47.4 \pm 15.7	43.4 \pm 15.6	46.4 \pm 16.7	47.2 \pm 17.6	45.9 \pm 12.9	47.3 \pm 14.8	49.1 \pm 14.3
Gallbladder	10.2 \pm 12.9	4.1 \pm 9.5	10.1 \pm 9.5	7.4 \pm 7.1	7.3 \pm 8.1	9.3 \pm 13.1	9.2 \pm 6.8	8.9 \pm 7.0	12.0 \pm 11.0
Esophagus	22.0 \pm 9.2	1.5 \pm 3.4	41.0 \pm 15.6	39.5 \pm 18.4	46.4 \pm 20.4	43.6 \pm 19.2	44.2 \pm 20.5	41.0 \pm 18.5	44.2 \pm 17.9
Pancreas	42.9 \pm 13.5	13.6 \pm 15.5	39.8 \pm 11.5	44.0 \pm 18.8	34.1 \pm 21.6	42.5 \pm 17.4	45.0 \pm 18.6	42.8 \pm 16.2	44.1 \pm 17.3
Duodenum	32.2 \pm 10.5	31.4 \pm 17.8	45.8 \pm 16.2	35.8 \pm 20.3	31.6 \pm 18.2	39.3 \pm 17.6	42.8 \pm 15.4	51.0 \pm 13.4	44.5 \pm 17.5
Colon	60.9 \pm 13.4	42.8 \pm 25.6	63.7 \pm 12.9	65.3 \pm 12.1	61.0 \pm 11.1	65.2 \pm 11.8	64.5 \pm 11.7	63.2 \pm 12.5	67.0 \pm 13.0
Intestine	58.7 \pm 11.6	27.7 \pm 21.1	63.1 \pm 13.0	61.8 \pm 16.8	62.0 \pm 17.0	61.9 \pm 17.6	65.2 \pm 13.1	63.9 \pm 14.0	62.6 \pm 11.0
Adrenal	29.8 \pm 17.0	10.5 \pm 15.6	36.8 \pm 16.1	30.5 \pm 18.8	32.2 \pm 19.7	35.0 \pm 19.7	38.1 \pm 15.7	38.6 \pm 13.5	40.4 \pm 17.7
Rectum	34.6 \pm 10.5	47.9 \pm 18.2	49.1 \pm 12.4	47.5 \pm 11.6	32.1 \pm 19.4	47.9 \pm 12.7	51.8 \pm 12.7	53.3 \pm 13.7	49.3 \pm 15.3
Bladder	33.9 \pm 15.2	45.8 \pm 23.0	49.5 \pm 18.1	55.3 \pm 21.1	49.6 \pm 20.1	52.3 \pm 22.2	50.8 \pm 20.4	55.4 \pm 16.9	55.4 \pm 16.9
Head of Femur L	43.7 \pm 10.8	71.9 \pm 22.4	71.8 \pm 8.5	80.2 \pm 8.7	84.1 \pm 8.9	83.1 \pm 8.9	81.6 \pm 9.1	77.9 \pm 8.5	76.7 \pm 16.7
Head of Femur R	36.2 \pm 10.9	55.3 \pm 29.4	63.8 \pm 13.3	70.9 \pm 12.5	75.9 \pm 13.7	74.0 \pm 14.0	70.2 \pm 14.2	68.3 \pm 13.9	69.4 \pm 14.4
Average	39.2 \pm 11.7	34.2 \pm 21.9	52.8 \pm 13.1	53.6 \pm 15.0	50.6 \pm 17.4	54.9 \pm 15.8	56.5 \pm 13.6	55.9 \pm 13.2	56.6 \pm 14.8

LAM significantly outperforms both nnDetection and MIU-VL on the StructSeg HaN and WORD datasets. Specifically, on the StructSeg HaN dataset, MedLAM achieved an average IoU of 48%, substantially surpassing nnDetection’s 16.1%. We also observed that MIU-VL was only able to delineate the entire body area regardless of the organ-specific prompt, highlighting a substantial gap between foundation models pre-trained on natural images and their applicability in the medical domain. These results also indicate that such natural image foundation models may struggle to provide meaningful localization in low-contrast medical images. In contrast, our MedLAM model, which incorporates strong medical domain knowledge, is capable of localizing any anatomical structure with just a few annotated examples, exceeding the performance of fully supervised models.

To be more specific, in the StructSeg HaN dataset, the organ with the largest average WD (Wall Distance) is the right parotid gland, which does not exceed 4mm. This suggests that MedLAM can perform highly accurate localization for head and neck organs. On the other hand, for the WORD dataset, the abdominal soft tissue organs have blurry boundaries and significant deformations, resulting in larger average WD values. However, the WD for each organ is generally within 15mm.

In summary, MedLAM exhibits robust localization performance and proves to be a versatile foundational model for localizing any type of structure in 3D medical imaging. For smaller organs, although the IoU scores are relatively lower, the subsequent preprocessing step of expanding the 3D bounding box ensures that these organs are adequately captured for segmentation. This makes the model practically applicable across a broad spectrum of organ sizes. This approach provides a pragmatic solution to the challenge of localizing smaller organs with MedLAM, thus achieving a balanced performance across different organ sizes.

4.4.2. Ablation Study of MedLAM

To assess the contributions of individual components within MedLAM, we conduct a series of experiments on the WORD dataset. Specifically, we evaluate MedLAM under the following conditions: 1) using only Unified Anatomical Mapping (UAM) for coarse localization; 2) relying solely on Multi Scale Similarity (MSS) for pinpointing the most similar point across the entire query image; 3) employing RDR for initial coarse localization, followed by MSS with and without features from each scale. The IoU scores obtained from these experiments are presented in Table 3. As can be observed, when using either RDR or MSS independently, the average IoU is below 50%, standing at 39.2% and 34.2%, respectively. This could be attributed to the following reasons: 1) RDR operates under the assumption of anatomical consistency, which may not hold true if the query volume undergoes significant deformation; 2) MSS focuses on the similarity of local features but lacks an understanding of global anatomical structures, making it susceptible to interference from other areas in the image that are similar to the query point. This results in the identification of false positives, as evidenced by the high variance in the MSS detection results.

However, when initiating with a coarse localization point identified by RDR and subsequently refining it with MSS, the detection accuracy is significantly improved. As shown in Table 3, the average IoU can be increased from 39.2% to 56.6% when using multi-scale features for MSS-based refining. Furthermore, using individual feature maps for F^i refining also improves the average IoU to over 50%, validating the effectiveness of combining global anatomical features with local pixel features.

4.5. Evaluation of MedLSAM

4.5.1. Effectness of MedLSAM

After validating the localization performance of MedLAM, we proceeded to examine the segmentation performance of the

Table 4: Comparison of segmentation performance between MedLAM-generated bounding box prompts and manually annotated prompts on the StructSeg Head-and-Neck dataset. Metrics include Dice Similarity Coefficient (DSC) and Hausdorff Distance (HD₉₅).

(a) StructSeg Head-and-Neck

Organs	DSC ↑ (mean±std %)				HD ₉₅ ↓ (mean±std mm)			
	MedLAM		Manual Prompt		MedLAM		Manual Prompt	
	SAM	MedSAM	SAM	MedSAM	SAM	MedSAM	SAM	MedSAM
Brain Stem	63.5±6.3	73.3 ± 5.0	66.2±2.7	75.9 ± 2.7	8.4±1.6	6.2 ± 1.2	8.6±1.0	6.1 ± 1.1
Eye L	64.5±6.5	69.3 ± 5.9	65.7±5.6	70.0 ± 4.6	8.0±1.5	5.8 ± 1.0	7.9±1.3	5.9 ± 1.1
Eye R	67.3±5.8	69.4 ± 5.5	68.9±4.8	69.1 ± 5.2	7.6±1.9	5.7 ± 1.2	7.4±1.2	6.2 ± 1.1
Lens L	15.9±7.8	16.0 ± 6.7	22.7 ± 5.6	19.2±3.5	8.0 ± 1.5	8.6±1.7	10.0±2.3	9.5 ± 1.3
Lens R	13.8±8.8	14.0 ± 5.5	22.8 ± 7.7	17.3±4.6	9.3 ± 1.5	9.6±1.3	9.7 ± 2.1	10.9±2.3
Opt Nerve L	23.7 ± 6.1	23.5±6.2	32.6±9.3	34.7 ± 5.4	9.0±1.7	8.6 ± 1.1	10.1±2.5	8.4 ± 1.3
Opt Nerve R	27.8 ± 10.2	26.3±6.6	28.5±6.7	32.4 ± 5.2	9.2±3.2	9.0 ± 1.4	11.3±2.2	9.4 ± 1.0
Opt Chiasma	11.4±10.6	14.4 ± 11.4	39.8±10.2	39.8 ± 8.1	10.2±1.4	8.8 ± 1.6	7.2±1.7	6.6 ± 1.2
Temporal Lobes L	28.2±15.2	78.3 ± 3.5	36.8±16.6	83.5 ± 1.9	16.4±3.5	9.0 ± 2.1	13.7±3.5	6.6 ± 1.4
Temporal Lobes R	24.1±17.4	78.0 ± 4.3	30.7±17.8	84.4 ± 1.4	18.2±4.2	10.1 ± 2.4	15.1±4.1	6.1 ± 2.5
Pituitary	12.5 ± 10.7	10.2±9.2	36.6 ± 16.2	27.5±12.5	8.7 ± 2.2	8.8±1.8	7.4 ± 2.0	10.0±3.6
Parotid Gland L	15.5±11.9	59.6 ± 6.5	29.5±7.7	64.4 ± 3.4	17.6±3.0	10.3 ± 1.9	16.0±1.9	9.3 ± 1.9
Parotid Gland R	17.2±9.9	57.1 ± 6.8	29.6±6.5	64.9 ± 5.0	19.8±5.0	13.5 ± 3.5	14.0±2.1	9.5 ± 1.6
Inner Ear L	40.4±11.8	42.3 ± 9.9	59.7±11.7	62.1 ± 9.7	9.4±1.7	7.6 ± 1.5	7.6±2.1	5.9 ± 1.8
Inner Ear R	48.9 ± 9.5	45.9±11.2	67.3 ± 10.4	66.9±6.1	8.4±1.7	7.0 ± 1.7	6.8±1.9	5.4 ± 1.2
Mid Ear L	64.6 ± 14.3	59.7±9.6	71.0 ± 11.7	67.5±6.3	7.9±2.6	7.7 ± 1.6	6.4±2.8	6.1 ± 1.1
Mid Ear R	64.7 ± 13.1	59.3±11.2	73.3 ± 7.7	65.0±8.9	8.4±2.4	7.6 ± 1.4	6.2 ± 1.9	6.6±1.2
TM Joint L	38.3±10.1	39.0 ± 10.9	59.7±12.8	61.2 ± 4.9	10.2±2.1	7.7 ± 1.6	6.8±1.9	6.0 ± 0.7
TM Joint R	41.5 ± 10.0	38.3±9.5	59.2±17.8	60.0 ± 7.7	9.6±1.6	8.1 ± 1.4	8.2±1.9	6.3 ± 1.1
Spinal Cord	27.9±8.3	34.7 ± 6.9	38.0±7.7	40.3 ± 6.1	15.5±2.7	13.3 ± 2.9	10.7±1.3	8.8 ± 0.9
Mandible L	78.0 ± 4.9	66.7±6.1	86.0 ± 2.1	76.8±4.7	11.1 ± 2.8	11.8±2.1	5.5 ± 1.7	9.0±4.5
Mandible R	71.4 ± 4.0	66.0±4.7	81.2 ± 2.7	75.0±4.5	22.6±4.7	12.3 ± 2.6	21.6±5.4	9.6 ± 3.5
Average	39.1±9.7	47.3 ± 7.4	50.3±9.2	57.2 ± 5.6	11.5±2.5	9.0 ± 1.8	9.9±2.2	7.6 ± 1.7

(b) WORD

Organs	DSC ↑ (mean±std %)				HD ₉₅ ↓ (mean±std mm)			
	MedLAM		Manual Prompt		MedLAM		Manual Prompt	
	SAM	MedSAM	SAM	MedSAM	SAM	MedSAM	SAM	MedSAM
Liver	66.0 ± 10.1	23.8±8.6	84.2 ± 6.3	46.6±14.7	53.6±10.4	51.5 ± 8.6	21.8 ± 11.9	36.8±11.6
Spleen	61.7 ± 14.4	36.3±13.2	85.3 ± 5.1	65.0±6.3	30.1 ± 16.1	30.5±14.4	10.8 ± 6.5	16.2±4.9
Kidney L	82.1 ± 16.0	70.7±18.8	92.1 ± 1.6	84.1±5.2	19.2±18.6	18.5 ± 16.9	6.1 ± 1.9	8.2±1.6
Kidney R	88.3 ± 4.8	77.3±6.2	92.9 ± 1.6	86.4±3.1	12.7 ± 5.7	13.4±4.1	6.0 ± 1.6	7.7±1.2
Stomach	44.6 ± 15.0	37.2±14.7	77.1±10.6	80.3 ± 4.7	50.1 ± 27.0	51.7±27.6	12.7±4.2	11.5 ± 3.6
Gallbladder	13.1 ± 17.3	10.2±13.4	72.7 ± 11.1	68.8±7.8	36.8±19.8	36.7 ± 20.4	6.0 ± 1.8	6.4±1.6
Esophagus	36.6 ± 14.7	27.8±12.9	67.0 ± 6.4	63.1±7.7	21.1±12.7	19.8 ± 11.6	6.9±4.0	6.7 ± 3.2
Pancreas	29.7 ± 14.1	21.4±9.7	64.4 ± 7.7	46.9±11.6	32.6 ± 13.5	33.1±10.8	15.9 ± 6.4	18.3±5.5
Duodenum	26.0 ± 11.4	21.1±7.0	54.1 ± 13.2	51.0±11.9	31.1±9.7	30.9 ± 10.4	16.0 ± 4.6	17.1±5.9
Colon	25.6±9.6	26.6 ± 8.9	41.8±6.8	44.1 ± 8.8	57.8 ± 17.8	60.6±17.8	49.4±15.3	49.1 ± 13.9
Intestine	37.5 ± 7.6	34.1±8.4	61.4 ± 6.9	52.5±8.0	47.1±10.5	44.1 ± 10.0	21.7±4.2	21.0 ± 4.0
Adrenal	3.3±3.9	10.0 ± 6.2	17.4±8.8	26.5 ± 5.9	30.8±8.7	29.9 ± 7.5	23.4±4.3	22.6 ± 2.7
Rectum	50.1 ± 17.9	46.0±18.7	75.5±4.0	80.0 ± 3.6	18.6±7.0	17.4 ± 7.2	7.6±0.9	4.8 ± 0.6
Bladder	65.3 ± 26.6	59.1±23.1	83.0 ± 15.5	82.9±8.0	20.5±10.2	19.8 ± 8.8	7.5±3.5	6.9 ± 2.0
Head of Femur L	81.7 ± 3.9	71.5±4.1	90.5 ± 2.7	80.3±2.8	16.6±3.3	14.9 ± 1.6	9.2 ± 4.7	12.3±2.0
Head of Femur R	80.1 ± 3.3	74.3±4.4	89.1 ± 3.4	83.2±2.7	19.5±2.6	13.4 ± 1.0	12.6±6.1	12.3 ± 7.7
Average	49.5 ± 11.9	40.5±11.1	71.8 ± 7.0	65.1±7.0	31.1±12.1	30.4 ± 11.2	14.6 ± 5.1	16.1±4.5

proposed MedLSAM framework. MedLSAM utilizes the localization information from MedLAM, together with either SAM or MedSAM, to perform segmentation tasks.

In our evaluation, we also included manually-annotated

bounding boxes to serve as the performance **upper bound** for SAM and MedSAM on the WORD and StructSeg HaN datasets. These were simulated based on the ground-truth masks, following the same approach used for generating bboxes in Med-

Table 5: Comparison of DSC scores \downarrow (mean \pm std%) for MedLSAM using different localization strategies on the StructSeg Head-and-Neck dataset: Whole-Patch Localization (WPL) and Sub-Patch Localization (SPL) with varying slice intervals n .

Organs	SAM				MedSAM			
	SPL			WPL	SPL			WPL
	$n = 6mm$	$n = 15mm$	$n = 30mm$	\times	$n = 6mm$	$n = 15mm$	$n = 30mm$	\times
Brain Stem	63.5 \pm 6.3	60.1 \pm 6.7	51.5 \pm 6.0	50.8 \pm 6.2	73.3 \pm 5.0	71.9 \pm 4.8	67.4 \pm 4.2	66.6 \pm 4.4
Eye L	64.5 \pm 6.5	61.2 \pm 6.7	61.2 \pm 6.7	61.2 \pm 6.7	69.3 \pm 5.9	66.4 \pm 5.7	66.4 \pm 5.7	66.4 \pm 5.7
Eye R	67.3 \pm 5.8	64.5 \pm 6.6	64.5 \pm 6.6	64.5 \pm 6.6	69.4 \pm 5.5	67.8 \pm 6.0	67.8 \pm 6.0	67.8 \pm 6.0
Lens L	15.9 \pm 7.8	15.7 \pm 7.7	15.7 \pm 7.7	15.7 \pm 7.7	16.0 \pm 6.7	15.8 \pm 6.7	15.8 \pm 6.7	15.8 \pm 6.7
Lens R	13.8 \pm 8.8	14.1 \pm 8.6	13.5 \pm 8.7	13.5 \pm 8.7	14.0 \pm 5.5	14.0 \pm 5.6	13.7 \pm 5.5	13.7 \pm 5.5
Opt Nerve L	23.7 \pm 6.1	23.9 \pm 5.9	23.7 \pm 6.1	23.7 \pm 6.1	23.5 \pm 6.2	23.6 \pm 6.2	23.5 \pm 6.2	23.5 \pm 6.2
Opt Nerve R	27.8 \pm 10.2	27.8 \pm 10.2	27.8 \pm 10.2	27.8 \pm 10.2	26.3 \pm 6.6	26.3 \pm 6.6	26.3 \pm 6.6	26.3 \pm 6.6
Opt Chiasma	11.4 \pm 10.6	11.4 \pm 10.6	11.4 \pm 10.6	11.4 \pm 10.6	14.4 \pm 11.4	14.4 \pm 11.4	14.4 \pm 11.4	14.4 \pm 11.4
Temporal Lobes L	28.2 \pm 15.2	21.7 \pm 14.8	25.7 \pm 13.4	25.7 \pm 13.4	78.3 \pm 3.5	73.1 \pm 3.5	71.0 \pm 3.6	71.0 \pm 3.6
Temporal Lobes R	24.1 \pm 17.4	18.2 \pm 17.7	18.5 \pm 16.4	18.5 \pm 16.4	78.0 \pm 4.3	75.9 \pm 3.1	71.0 \pm 3.5	71.0 \pm 3.5
Pituitary	12.5 \pm 10.7	12.6 \pm 10.7	12.6 \pm 10.7	12.6 \pm 10.7	10.2 \pm 9.2	10.3 \pm 9.4	10.3 \pm 9.4	10.3 \pm 9.4
Parotid Gland L	15.5 \pm 11.9	10.4 \pm 9.6	5.5 \pm 6.6	5.5 \pm 6.6	59.6 \pm 6.5	56.4 \pm 6.6	48.1 \pm 7.3	48.1 \pm 7.3
Parotid Gland R	17.2 \pm 9.9	13.1 \pm 10.5	7.7 \pm 7.7	7.7 \pm 7.7	57.1 \pm 6.8	54.6 \pm 6.8	45.3 \pm 7.8	45.3 \pm 7.8
Inner Ear L	40.4 \pm 11.8	40.4 \pm 11.8	40.4 \pm 11.8	40.4 \pm 11.8	42.3 \pm 9.9	42.3 \pm 9.9	42.3 \pm 9.9	42.3 \pm 9.9
Inner Ear R	48.9 \pm 9.5	48.9 \pm 9.5	48.9 \pm 9.5	48.9 \pm 9.5	45.9 \pm 11.2	45.9 \pm 11.2	45.9 \pm 11.2	45.9 \pm 11.2
Mid Ear L	64.6 \pm 14.3	62.3 \pm 14.7	62.3 \pm 14.7	62.3 \pm 14.7	59.7 \pm 9.6	55.8 \pm 10.0	55.7 \pm 10.0	55.7 \pm 10.0
Mid Ear R	64.7 \pm 13.1	62.4 \pm 13.1	62.4 \pm 13.0	62.4 \pm 13.0	59.3 \pm 11.2	53.6 \pm 12.1	53.4 \pm 11.9	53.4 \pm 11.9
TM Joint L	38.3 \pm 10.1	38.3 \pm 10.1	38.3 \pm 10.1	38.3 \pm 10.1	39.0 \pm 10.9	39.0 \pm 10.9	39.0 \pm 10.9	39.0 \pm 10.9
TM Joint R	41.5 \pm 10.0	41.5 \pm 10.0	41.5 \pm 10.0	41.5 \pm 10.0	38.3 \pm 9.5	38.3 \pm 9.5	38.3 \pm 9.5	38.3 \pm 9.5
Spinal Cord	27.9 \pm 8.3	27.7 \pm 8.2	27.8 \pm 8.3	7.8 \pm 2.9	34.7 \pm 6.9	34.7 \pm 6.9	34.7 \pm 6.9	11.7 \pm 3.9
Mandible L	78.0 \pm 4.9	78.0 \pm 5.2	68.0 \pm 6.2	47.0 \pm 5.3	66.7 \pm 6.1	66.7 \pm 5.2	46.7 \pm 5.8	22.9 \pm 4.1
Mandible R	71.4 \pm 4.0	69.0 \pm 4.4	58.5 \pm 3.9	40.2 \pm 4.6	66.0 \pm 4.7	64.7 \pm 4.9	48.2 \pm 5.0	25.9 \pm 3.2
Average	39.1 \pm 9.7	37.4 \pm 9.7	35.8 \pm 9.2	33.1 \pm 9.1	47.3 \pm 7.4	46.0 \pm 7.4	43.0 \pm 7.5	39.8 \pm 7.2

SAM. During inference, a bbox prompt was generated from each ground-truth mask, with a random perturbation of 0-20 pixels introduced to mimic the potential inaccuracies that would be present in manually-drawn bboxes.

It can be observed that MedLSAM demonstrates performance closely approximating that achieved with manual prompts for many organs. For instance, in the case of the brain stem, MedLSAM attains a DSC score of 73.3%, while the manual prompt reaches 75.9%. However, for certain abdominal organs with substantial shape variability, such as the pancreas, the performance gap between MedLSAM and manual prompts is more significant, with a DSC score difference reaching up to 35%. Fig. 6 visually presents the results of using MedLSAM for localization and segmentation tasks on both datasets.

Overall, MedLSAM performs more comparably to manual prompts in the case of head and neck organs, representing a pioneering and effective attempt towards fully automating the use of SAM in medical imaging.

4.5.2. Ablation study of SPL

To validate the effectiveness of Sub-Patch Localization (SPL), we conducted experiments on the StructSeg HaN dataset, comparing the performance of SPL at different sub-patch intervals n mm against the Whole-Patch Localization (WPL) approach. As described in Sec. 4.2, the WPL method relies on the extreme coordinates of the entire organ for localization. On the other hand, SPL employs a more granular ap-

proach by segmenting the organ into multiple sub-patches at intervals of n mm.

As shown in Table 5, it is evident that the SPL approach consistently outperforms WPL. Notably, for organs with significant morphological variations, such as the brain stem and spinal cord, the DSC score improves by more than 7% and 20%, respectively. Moreover, when n is relatively small, SPL enables finer-grained localization by concentrating on smaller, more specific portions of the organ. This results in bounding boxes that better approximate the organ’s actual shape at each slice, thereby enhancing the accuracy of the subsequent segmentation process.

5. Discussion & Conclusions

In this study, we have introduced MedLSAM, the first completely automated, two-stage medical adaptation of the SAM model, designed to significantly alleviate the annotation workload in the segmentation of medical images. The first stage, MedLAM, serves as a pioneering localization foundation model, capable of precisely identifying anatomical structures in 3D medical images. The second stage leverages the strength of SAM and its medical adaptations for meticulous image segmentation. Together, these components form a fully automated pipeline that significantly reduces the reliance on manual annotations and annotated data.

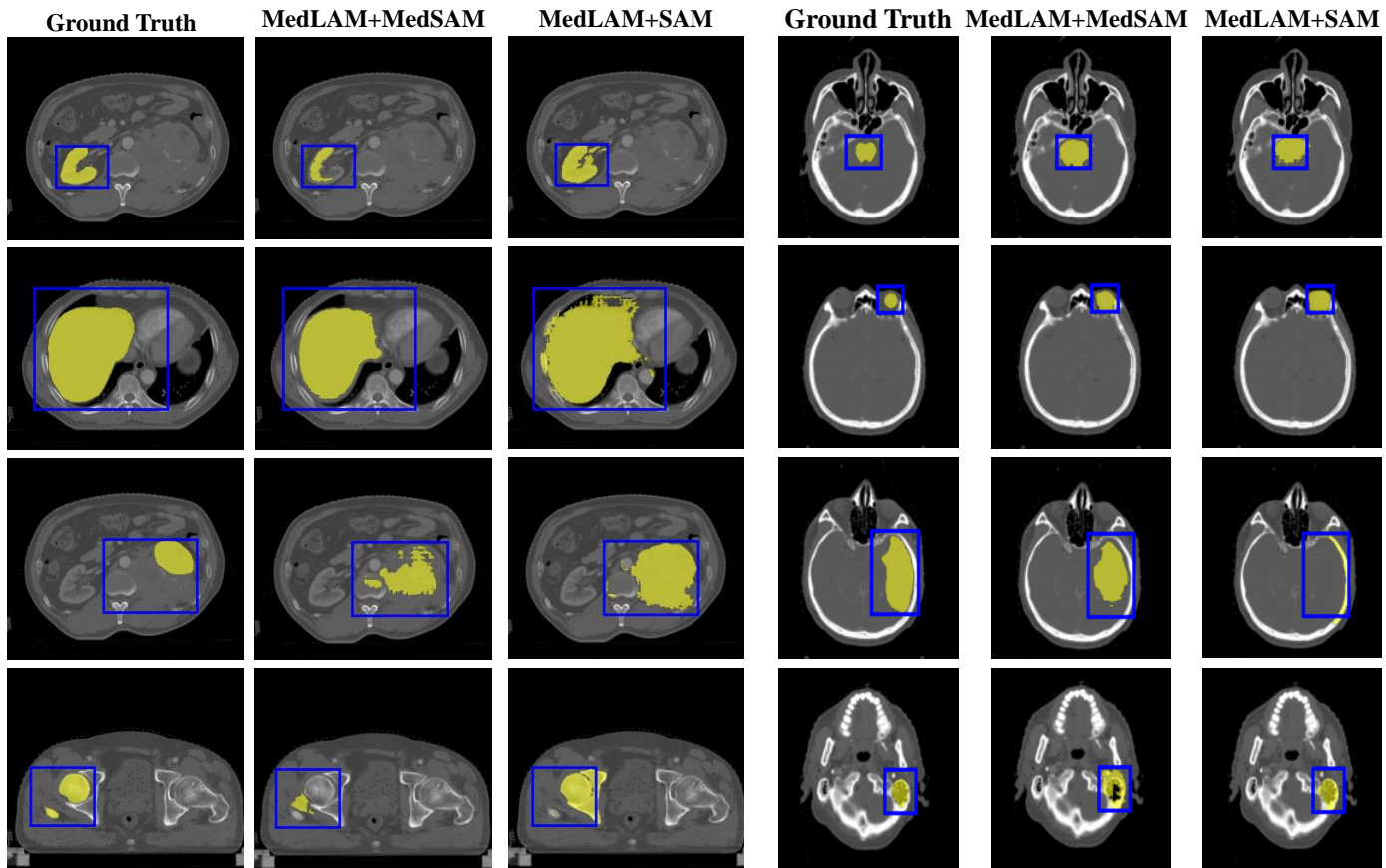


Fig. 6: Visualization examples of segmentation results on WORD and StructSeg Head-and-Neck datasets using pre-trained MedSAM and SAM, post landmark localization with MedLAM.

This endeavor was fueled by the observation that the spatial distributions of organs across different patients maintain strong similarities. Consequently, MedLAM was designed to project every part of the scans onto a shared 3D latent coordinate system, accurately localizing target anatomical parts within the body. Coupling this approach with SAM's segmentation capabilities led to an efficient and accurate process for image segmentation.

Moreover, MedLSAM demonstrated its effectiveness across two 3D datasets covering 38 different organs, providing robust evidence of its versatility. Importantly, this automated approach is not burdened by an increased annotation workload as data size increases. It also holds promise for direct integration with potential future 3D SAM models in the medical field, which could further enhance its performance and utility.

Acknowledgments

References

Antonelli, M., Reinke, A., Bakas, S., Farahani, K., Kopp-Schneider, A., Landman, B.A., Litjens, G., Menze, B., Ronneberger, O., Summers, R.M., et al., 2022. The medical segmentation decathlon. *Nature communications* 13, 4128.

Armato III, S.G., McLennan, G., Bidaut, L., McNitt-Gray, M.F., Meyer, C.R., Reeves, A.P., Zhao, B., Aberle, D.R., Henschke, C.I., Hoffman, E.A., et al., 2011. The lung image database consortium (lidc) and image database resource initiative (idri): a completed reference database of lung nodules on ct scans. *Medical physics* 38, 915–931.

Azizi, S., Culp, L., Freyberg, J., Mustafa, B., Baur, S., Kornblith, S., Chen, T., MacWilliams, P., Mahdavi, S.S., Wulczyn, E., et al., 2022. Robust and efficient medical imaging with self-supervision. *arXiv preprint arXiv:2205.09723*.

Baumgartner, M., Jäger, P.F., Isensee, F., Maier-Hein, K.H., 2021. nndetection: a self-configuring method for medical object detection, in: *Medical Image Computing and Computer Assisted Intervention–MICCAI 2021: 24th International Conference, Strasbourg, France, September 27–October 1, 2021, Proceedings, Part V 24*, Springer. pp. 530–539.

Bilic, P., Christ, P., Li, H.B., Vorontsov, E., Ben-Cohen, A., Kaissis, G., Szeskin, A., Jacobs, C., Mamani, G.E.H., Chartrand, G., et al., 2023. The liver tumor segmentation benchmark (lits). *Medical Image Analysis* 84, 102680.

Bo, Z.H., Qiao, H., Tian, C., Guo, Y., Li, W., Liang, T., Li, D., Liao, D., Zeng, X., Mei, L., et al., 2021. Toward human intervention-free clinical diagnosis of intracranial aneurysm via deep neural network. *Patterns* 2, 100197.

Butoi, V.I., Ortiz, J.J.G., Ma, T., Sabuncu, M.R., Gutttag, J., Dalca, A.V., 2023. Universeg: Universal medical image segmentation. *arXiv preprint arXiv:2304.06131*.

Caron, M., Touvron, H., Misra, I., Jégou, H., Mairal, J., Bojanowski, P., Joulin, A., 2021. Emerging properties in self-supervised vision transformers, in: *Proceedings of the IEEE/CVF international conference on computer vision*, pp. 9650–9660.

Chen, C., 2022. Miccai 2022 mela challenge: Mediastinal lesion analysis. URL: <https://mela.grand-challenge.org/Dataset/>.

Chen, X., Lian, C., Deng, H.H., Kuang, T., Lin, H.Y., Xiao, D., Gateno, J., Shen, D., Xia, J.J., Yap, P.T., 2021. Fast and accurate craniomaxillofacial landmark detection via 3d faster r-cnn. *IEEE Transactions on Medical Imaging* 40, 3867–3878.

Cheng, D., Qin, Z., Jiang, Z., Zhang, S., Lao, Q., Li, K., 2023. Sam on medical images: A comprehensive study on three prompt modes. *arXiv preprint arXiv:2305.00035*.

Dai, J., Li, Y., He, K., Sun, J., 2016. R-fcn: Object detection via region-based fully convolutional networks. *Advances in neural information processing*

- systems 29.
- Dosovitskiy, A., Beyer, L., Kolesnikov, A., Weissenborn, D., Zhai, X., Unterthiner, T., Dehghani, M., Minderer, M., Heigold, G., Gelly, S., et al., 2020. An image is worth 16x16 words: Transformers for image recognition at scale. arXiv preprint arXiv:2010.11929 .
- Gatidis, S., Hepp, T., Früh, M., La Fougère, C., Nikolaou, K., Pfannenber, C., Schölkopf, B., Küstner, T., Cyran, C., Rubin, D., 2022. A whole-body fdg-pet/ct dataset with manually annotated tumor lesions. *Scientific Data* 9, 601.
- Grossberg, A.J., Mohamed, A.S., Elhalawani, H., Bennett, W.C., Smith, K.E., Nolan, T.S., Williams, B., Chamchod, S., Heukelom, J., Kantor, M.E., et al., 2018. Imaging and clinical data archive for head and neck squamous cell carcinoma patients treated with radiotherapy. *Scientific data* 5, 1–10.
- He, K., Gkioxari, G., Dollár, P., Girshick, R., 2017. Mask r-cnn, in: *Proceedings of the IEEE international conference on computer vision*, pp. 2961–2969.
- He, K., Zhang, X., Ren, S., Sun, J., 2016. Deep residual learning for image recognition, in: *Proceedings of the IEEE conference on computer vision and pattern recognition*, pp. 770–778.
- He, S., Bao, R., Li, J., Grant, P.E., Ou, Y., 2023a. Accuracy of segment-anything model (sam) in medical image segmentation tasks. arXiv preprint arXiv:2304.09324 .
- He, S., Bao, R., Li, J., Stout, J., Bjornerud, A., Grant, P.E., Ou, Y., 2023b. Computer-vision benchmark segment-anything model (sam) in medical images: Accuracy in 12 datasets. arXiv preprint arXiv:2304.09324 .
- Heller, N., Isensee, F., Maier-Hein, K.H., Hou, X., Xie, C., Li, F., Nan, Y., Mu, G., Lin, Z., Han, M., et al., 2020. The state of the art in kidney and kidney tumor segmentation in contrast-enhanced ct imaging: Results of the kits19 challenge. *Medical Image Analysis* , 101821.
- Huang, Y., Yang, X., Liu, L., Zhou, H., Chang, A., Zhou, X., Chen, R., Yu, J., Chen, J., Chen, C., et al., 2023a. Segment anything model for medical images? arXiv preprint arXiv:2304.14660 .
- Huang, Z., Wang, H., Deng, Z., Ye, J., Su, Y., Sun, H., He, J., Gu, Y., Gu, L., Zhang, S., et al., 2023b. Stu-net: Scalable and transferable medical image segmentation models empowered by large-scale supervised pre-training. arXiv preprint arXiv:2304.06716 .
- Humpire-Mamani, G.E., Setio, A.A.A., Van Ginneken, B., Jacobs, C., 2018. Efficient organ localization using multi-label convolutional neural networks in thorax-abdomen ct scans. *Physics in Medicine & Biology* 63, 085003.
- Hussain, M.A., Hamarneh, G., Garbi, R., 2021. Cascaded regression neural nets for kidney localization and segmentation-free volume estimation. *IEEE Transactions on Medical Imaging* 40, 1555–1567.
- Ji, Y., Bai, H., Yang, J., Ge, C., Zhu, Y., Zhang, R., Li, Z., Zhang, L., Ma, W., Wan, X., et al., 2022. Amos: A large-scale abdominal multi-organ benchmark for versatile medical image segmentation. arXiv preprint arXiv:2206.08023 .
- Kingma, D.P., Ba, J., 2014. Adam: A method for stochastic optimization. arXiv preprint arXiv:1412.6980 .
- Kirillov, A., Mintun, E., Ravi, N., Mao, H., Rolland, C., Gustafson, L., Xiao, T., Whitehead, S., Berg, A.C., Lo, W.Y., et al., 2023. Segment anything. arXiv preprint arXiv:2304.02643 .
- Kwan, J.Y.Y., Su, J., Huang, S.H., Ghorai, L.S., Xu, W., Chan, B., Yip, K.W., Giuliani, M., Bayley, A., Kim, J., et al., 2018. Radiomic biomarkers to refine risk models for distant metastasis in hpv-related oropharyngeal carcinoma. *International Journal of Radiation Oncology* Biology* Physics* 102, 1107–1116.
- Lee, R.S., Gimenez, F., Hoogi, A., Miyake, K.K., Gorovoy, M., Rubin, D.L., 2017. A curated mammography data set for use in computer-aided detection and diagnosis research. *Scientific data* 4, 1–9.
- Lei, W., Wang, H., Gu, R., Zhang, S., Zhang, S., Wang, G., 2019. Deepigeosv2: Deep interactive segmentation of multiple organs from head and neck images with lightweight cnns, in: *Large-Scale Annotation of Biomedical Data and Expert Label Synthesis and Hardware Aware Learning for Medical Imaging and Computer Assisted Intervention: International Workshops, LABELS 2019, HAL-MICCAI 2019, and CuRIOUS 2019, Held in Conjunction with MICCAI 2019, Shenzhen, China, October 13 and 17, 2019, Proceedings 4*, Springer. pp. 61–69.
- Lei, W., Xu, W., Gu, R., Fu, H., Zhang, S., Zhang, S., Wang, G., 2021. Contrastive learning of relative position regression for one-shot object localization in 3d medical images, in: *Medical Image Computing and Computer Assisted Intervention–MICCAI 2021: 24th International Conference, Strasbourg, France, September 27–October 1, 2021, Proceedings, Part II 24*, Springer. pp. 155–165.
- Li, L.H., Zhang, P., Zhang, H., Yang, J., Li, C., Zhong, Y., Wang, L., Yuan, L., Zhang, L., Hwang, J.N., et al., 2022. Grounded language-image pre-training, in: *Proceedings of the IEEE/CVF Conference on Computer Vision and Pattern Recognition*, pp. 10965–10975.
- Liu, J., Zhang, Y., Chen, J.N., Xiao, J., Lu, Y., Landman, B.A., Yuan, Y., Yuille, A., Tang, Y., Zhou, Z., 2023. Clip-driven universal model for organ segmentation and tumor detection. arXiv preprint arXiv:2301.00785 .
- Liu, Z., Mao, H., Wu, C.Y., Feichtenhofer, C., Darrell, T., Xie, S., 2022. A convnet for the 2020s, in: *Proceedings of the IEEE/CVF conference on computer vision and pattern recognition*, pp. 11976–11986.
- Lowe, V.J., Duan, F., Subramaniam, R.M., Sicks, J.D., Romanoff, J., Bartel, T., Yu, J.Q.M., Nussenbaum, B., Richmon, J., Arnold, C.D., et al., 2019. Multicenter trial of [18f] fluorodeoxyglucose positron emission tomography/computed tomography staging of head and neck cancer and negative predictive value and surgical impact in the n0 neck: results from acrin 6685. *Journal of Clinical Oncology* 37, 1704.
- Luo, X., Liao, W., Xiao, J., Chen, J., Song, T., Zhang, X., Li, K., Metaxas, D.N., Wang, G., Zhang, S., 2022. Word: A large scale dataset, benchmark and clinical applicable study for abdominal organ segmentation from ct image. *Medical Image Analysis* 82, 102642.
- Ma, J., Wang, B., 2023. Segment anything in medical images. arXiv preprint arXiv:2304.12306 .
- Ma, J., Zhang, Y., Gu, S., An, X., Wang, Z., Ge, C., Wang, C., Zhang, F., Wang, Y., Xu, Y., et al., 2022. Fast and low-gpu-memory abdomen ct organ segmentation: the flare challenge. *Medical Image Analysis* 82, 102616.
- Mazurowski, M.A., Dong, H., Gu, H., Yang, J., Konz, N., Zhang, Y., 2023. Segment anything model for medical image analysis: an experimental study. arXiv preprint arXiv:2304.10517 .
- Navarro, F., Sasahara, G., Shit, S., Sekuboyina, A., Ezhov, I., Peeken, J.C., Combs, S.E., Menze, B.H., 2022. A unified 3d framework for organs-at-risk localization and segmentation for radiation therapy planning, in: *2022 44th Annual International Conference of the IEEE Engineering in Medicine & Biology Society (EMBC), IEEE*. pp. 1544–1547.
- Navarro, F., Sekuboyina, A., Waldmannstetter, D., Peeken, J.C., Combs, S.E., Menze, B.H., 2020. Deep reinforcement learning for organ localization in ct, in: *Medical Imaging with Deep Learning*, PMLR. pp. 544–554.
- Ouyang, L., Wu, J., Jiang, X., Almeida, D., Wainwright, C., Mishkin, P., Zhang, C., Agarwal, S., Slama, K., Ray, A., et al., 2022. Training language models to follow instructions with human feedback. *Advances in Neural Information Processing Systems* 35, 27730–27744.
- Qin, Z., Yi, H., Lao, Q., Li, K., 2022. Medical image understanding with pretrained vision language models: A comprehensive study. arXiv preprint arXiv:2209.15517 .
- Qin, Z., Yi, H.H., Lao, Q., Li, K., 2023. Medical image understanding with pretrained vision language models: A comprehensive study, in: *The Eleventh International Conference on Learning Representations*. URL: <https://openreview.net/forum?id=txlWziucE5W>.
- Radford, A., Kim, J.W., Hallacy, C., Ramesh, A., Goh, G., Agarwal, S., Sastry, G., Askell, A., Mishkin, P., Clark, J., et al., 2021. Learning transferable visual models from natural language supervision, in: *International conference on machine learning*, PMLR. pp. 8748–8763.
- Redmon, J., Divvala, S., Girshick, R., Farhadi, A., 2016. You only look once: Unified, real-time object detection, in: *Proceedings of the IEEE conference on computer vision and pattern recognition*, pp. 779–788.
- Ren, S., He, K., Girshick, R., Sun, J., 2015. Faster r-cnn: Towards real-time object detection with region proposal networks. *Advances in neural information processing systems* 28.
- Revel, M.P., Boussouar, S., de Margerie-Mellon, C., Saab, I., Lapotre, T., Mompont, D., Chassagnon, G., Milon, A., Lederlin, M., Bennani, S., et al., 2021. Study of thoracic ct in covid-19: the stoic project. *Radiology* 301, E361–E370.
- Sun, Y., Luebbers, H.T., Agbaje, J.O., Schepers, S., Vrielinck, L., Lambrichts, I., Politis, C., 2013. Validation of anatomical landmarks-based registration for image-guided surgery: an in-vitro study. *Journal of Cranio-Maxillofacial Surgery* 41, 522–526.
- Vallieres, M., Kay-Rivest, E., Perrin, L.J., Liem, X., Furstoss, C., Aerts, H.J., Khauam, N., Nguyen-Tan, P.F., Wang, C.S., Sultanem, K., et al., 2017. Radiomics strategies for risk assessment of tumour failure in head-and-neck cancer. *Scientific reports* 7, 10117.
- Vorontsov, E., Bozkurt, A., Casson, A., Shaikovski, G., Zelechowski, M., Liu, S., Mathieu, P., Eck, A.v., Lee, D., Viret, J., et al., 2023. Virchow: A million-slide digital pathology foundation model. arXiv preprint arXiv:2309.07778

- Wan, K., Li, L., Jia, D., Gao, S., Qian, W., Wu, Y., Lin, H., Mu, X., Gao, X., Wang, S., et al., 2023. Multi-target landmark detection with incomplete images via reinforcement learning and shape prior embedding. *Medical Image Analysis* , 102875.
- Wang, G., Wu, J., Luo, X., Liu, X., Li, K., Zhang, S., 2023. Mis-fm: 3d medical image segmentation using foundation models pretrained on a large-scale unannotated dataset. *arXiv preprint arXiv:2306.16925* .
- Wang, G., Zuluaga, M.A., Li, W., Pratt, R., Patel, P.A., Aertsen, M., Doel, T., David, A.L., Deprest, J., Ourselin, S., et al., 2018. Deepigeos: a deep interactive geodesic framework for medical image segmentation. *IEEE transactions on pattern analysis and machine intelligence* 41, 1559–1572.
- Wu, J., Fu, R., Fang, H., Liu, Y., Wang, Z., Xu, Y., Jin, Y., Arbel, T., 2023. Medical sam adapter: Adapting segment anything model for medical image segmentation. *arXiv preprint arXiv:2304.12620* .
- Xu, X., Zhou, F., Liu, B., Fu, D., Bai, X., 2019. Efficient multiple organ localization in ct image using 3d region proposal network. *IEEE transactions on medical imaging* 38, 1885–1898.
- Yan, K., Wang, X., Lu, L., Summers, R.M., 2018. Deeplesion: automated mining of large-scale lesion annotations and universal lesion detection with deep learning. *Journal of medical imaging* 5, 036501–036501.
- Yao, Q., Quan, Q., Xiao, L., Kevin Zhou, S., 2021. One-shot medical landmark detection, in: *Medical Image Computing and Computer Assisted Intervention–MICCAI 2021: 24th International Conference, Strasbourg, France, September 27–October 1, 2021, Proceedings, Part II* 24, Springer. pp. 177–188.
- Zhang, G., Jiang, S., Yang, Z., Gong, L., Ma, X., Zhou, Z., Bao, C., Liu, Q., 2018. Automatic nodule detection for lung cancer in ct images: A review. *Computers in biology and medicine* 103, 287–300.
- Zhang, H., Zhang, P., Hu, X., Chen, Y.C., Li, L., Dai, X., Wang, L., Yuan, L., Hwang, J.N., Gao, J., 2022. Glipv2: Unifying localization and vision-language understanding. *Advances in Neural Information Processing Systems* 35, 36067–36080.
- Zhang, K., Liu, D., 2023. Customized segment anything model for medical image segmentation. *arXiv preprint arXiv:2304.13785* .
- Zhang, S., Metaxas, D., 2023. On the challenges and perspectives of foundation models for medical image analysis. *arXiv preprint arXiv:2306.05705* .
- Zhang, Y., Jiao, R., 2023. How segment anything model (sam) boost medical image segmentation? *arXiv preprint arXiv:2305.03678* .
- Zhou, Y., Chia, M.A., Wagner, S.K., Ayhan, M.S., Williamson, D.J., Struyven, R.R., Liu, T., Xu, M., Lozano, M.G., Woodward-Court, P., et al., 2023. A foundation model for generalizable disease detection from retinal images. *Nature* , 1–8.